Full length article

Data-driven multiscale simulation of solid-state batteries via machine learning

Armin Asheri [a,b,*], Mozhdeh Fathidoost [b], Vedran Glavas [a], Shahed Rezaei [b,**], Bai-Xiang Xu [b,**]

[a] *Volkswagen Group, Berliner Ring 2, 38436 Wolfsburg, Germany*
[b] *Mechanics of Functional Materials Division, Institute of Materials Science, Technische Universität Darmstadt, 64287 Darmstadt, Germany*

ARTICLE INFO

ABSTRACT

The battery cell performance is determined by electro-chemo-mechanical mechanisms on different length scales. Though there exist multi-field multiscale simulation frameworks, the high computation cost prevents their wide application. It is even more challenging when it comes to all-solid-state batteries where the influence of the interface damage and delamination between the solid electrolyte and cathode active material plays a critical role in cell performance and degradation. In this contribution, we propose a novel multiscale strategy based on large datasets and machine learning. Thereby a large dataset of simulations is obtained at the microscale for electrolyte-active material two-phase representative elements by employing a coupled chemo-mechanical model with varying materials and state variables. The data is then used to train a surrogate model based on a neural network. The surrogate model is capable of predicting the microscopic behavior with respect to the theories and thermodynamics law but much more efficient to access soon after it is trained sufficiently well. The surrogate model is then employed in the multi-field two-level framework to predict the cell performance, particularly the impact of interface damage on the capacity loss. By comparing it with the original multi-field two-level simulation results, the data-driven multiscale strategy is shown to be promising with high accuracy and efficiency, demonstrating the large potential of data-driven multiscale simulations for lithium-ion battery design.

1. Introduction

Lithium-ion batteries (LIB) have shown great potential in energy storage applications such as portable electronic devices and electric vehicles. LIBs also have a major role in developing solutions to control global warming and climate change. Therefore, the market for LIBs is growing and the demand for more efficient battery systems with higher energy densities has made them an interesting research topic. Recently, solid-state lithium batteries which use a solid electrolyte (SE) instead of a liquid one, as in conventional LIBs, have gained much interest. These batteries can achieve higher energy densities and have better safety properties than the traditional ones [1,2]. All-solid-state batteries (ASSB) make it possible to use Li metal in the anode, which has a significant effect on increasing the battery energy density [3]. The known cathode active materials include $LiCoO_2$, $LiMn_2O_4$, $LiNi_xMn_yCo_zO_2$ (NMC), and $LiFePO_4$. Some examples of solid electrolytes are $Li_7La_3Zr_2O_{12}$ (LLZO), $Li_{0.33}La_{0.57}TiO_3$ (LLTO), $Li_xPO_yN_z$, and $Li_{10}GeP_2S_{12}$. Apart from the mentioned upsides for ASSB, several aspects such as the formation of cracks and fractures within ASSB might hinder their application. In the composite cathode, delamination between the active material (AM) and the solid-state electrolyte is one major issue that is observed in the experimental studies [4]. During cycles of charge and discharge, the concentration profile changes severely within AM and SE. Different volume changes in response to a change in concentration within the AM and the SE results in the formation of a gap at their interface. The latter is also known as interface delamination (see also [2,4–6]). It is worth mentioning that even for damage progression in battery material, we have different categories and failure modes. For example, one can mention intergranular and transgranular fracture inside AM particles, as well as in the SE [7–10]. For a comprehensive overview of various failure mechanisms in ASSB see also [1,11,12].

The above arguments make it clear that for better performance at the cell level, we require insight from the microscale. In other words, we are dealing with a multiscale and multiphysics problem. As it is reviewed in the following, the existing scaling strategies either assume strong simplification on the microscale or are computationally expensive. Often, one can sacrifice some details to speed up the process

---

of transforming the information between different scales. Nevertheless, even some small details might severely change our predictions and therefore make the whole process questionable. The focus of the current study is to employ an alternative solution based on data-driven methods and machine learning algorithms to connect micro and macro scale. We intend to show the efficient yet accurate modeling of ASSBs under consideration of the electro-chemo-mechanical effects at the microscale. In particular, we address the delamination at the interface of AM and SE and its impact on the cell performance. In the following the state-of-the-art approaches for modeling Li-ion batteries are reviewed.

1.1. State of the art in electro-chemo-mechanical battery modeling

The predictions from an accurate model provide a tool to propose new designs for a better performance of battery systems [13]. On the lower scale (micro-level), the active material and its connection with the solid electrolyte is of interest. At this level, a chemo-mechanically coupled formulation is necessary. Moreover, electrochemical reactions take place at the interface of AM and SE. The latter point has to be also coupled with the interface delamination between the active material and solid electrolyte. On the battery cell level, the mass and charge transport along with the cell thickness should be resolved. In the following we briefly review some recent progress on the modeling aspect of these two involved scales.

On the micro-level, the electro-chemo-mechanical models provide insights into understanding the interplay of diffusion, deformation, phase transformation, and fracture in the active material particles. Furthermore, modeling damage and fracture are of great importance for which researchers have developed various methods through the years. See [14] for an overview. The fracture models should be also coupled with the electrochemical aspect of the problem consistently. Zhang et al. [15] implemented a cohesive crack modeling to simulate the intergranular fracture in cathode active particles. They showed that fracture energy has a big impact on crack formation. Bucci et al. [16], presented an electro-chemo-mechanical model using a cohesive zone (CZ) model. Xu et al. [17] performed numerical investigations on the corrosive fracture of cathode active material with a coupled diffusion, large deformation, and cohesive zone model. Singh and Pal [18] developed a chemo-mechanical cohesive zone model in a multi-physics framework to study the fracture of polycrystalline active material particles. Sultanova and Figiel [19] developed a model by coupling mass transport with linear momentum balance equations where the interfacial traction-separation law is introduced at the interface of AM and SE (see also [20]). Bai et al. [21] presented a cohesive zone model coupled with diffusion and phase separation and studied intergranular fracture in the polycrystalline active material. Rezaei et al. [11] further developed the cohesive zone model for mode-dependent fracture and its influence on the species flux. The authors also applied the model for studies on cracking in ASSB. There are also other fracture models based on the diffuse damage zone which has some advantages when it comes to arbitrary cracking [14]. Klinsmann et al. [22] studied the crack growth during lithiation and delithiation using a phase-field fracture approach. Xu et al. [23] developed a finite strain phase-field fracture model which includes phase separation, fracture, and the related electrochemical reaction. See also investigations by [24–26].

Several models have been introduced to describe the LIBs behavior and performance at the cell level. These models mostly focus on the Li^+ transport and the charge balance through the cell. The pseudo-two-dimensional (P2D) model first introduced by Doyle et al. [27] was used to study the cell performance of LIBs, by modeling the Li^+ transport at the macroscale in 1D based on the porous electrode theory. They modeled the diffusion of the Li in the active material in the radial direction of the spherical active particles based on Fick's law. Christensen [28] further developed the P2D model to capture the effect of pressure on the cell performance and the diffusion-induced stress. Wolff et al. [29] implemented the P2D model for ASSBs and

investigated the single ion conducting and binary solid electrolytes and their cell performances. Golmon et al. [30] introduced a multiscale approach to simulate the cell behavior, whereby homogenization techniques were used to describe the stress state at the cell level. Bai et al. [31] also introduced a concurrent multiscale framework based on the two-level finite element methods (FE^2) to investigate the cell performance while considering large deformations and phase separation in the active material particles at the microscale. They introduced the multiphysics modeling of the active material particle to the P2D cell model, and also investigated the effect of particle shape, mechanics and phase separation on the cell performance by studying different models at the particle level. Kumbhar et al. [32] also introduced a mesoscale-continuum framework for modeling LIB's charging and discharging through a semi-concurrent multiscale framework. Several rigorous microstructure-based battery cell models have also been introduced and implemented to simulate the cell performance, such as the work of Fathiannasab et al. [33], where the authors reconstructed the microstructure of the ASSB battery electrode from tomography data to simulate the galvanostatic discharge performance of it. Wegener et al. [34] also implemented a three-dimensional single particle electrochemical model, where they considered more details from the microstructure, namely the orientation of the primary cathode active material particles, in the simulation.

The reviewed literature shows the importance and progress in the modeling and addressing of the multiphysics and multiscale nature of fracture in ASSBs and its effect on the overall cell performance. On the microscale, it is essential to utilize models which take into account a two-way consistent coupling between degradation mechanism and mass transport. For example, the influence of the damage on the species flux is very important especially when it comes to degradation under a cyclic loading/unloading. On the macroscale, most of the models proposed to describe the cell performance are usually simplified that the details of the active material including the fracture at the active material are ignored. On the other hand, the multiscale models which account for the microscale details, are usually costly and inefficient. Therefore, there is a need for a multiscale approach that is computationally efficient and also covers the microscale details.

1.2. AI based multiscaling

The multilevel finite element method, FE^2, is widely used to simulate the multiscale mechanical behavior of structures [35–37], especially for the composite material, where a heterogeneous multiphase microstructure is considered at the microscale. In this method, each integration point of the discretized macroscale is associated with a microscale finite element problem. FE^2 method is implemented in multiscale battery cell simulation as well [30,31]. For each arbitrary point in the composite cathode, a representative cathode active material particle is considered, the details of which are treated at the microscale. Despite the high accuracy which is obtained by utilizing FE^2 method, they are known to be computationally costly. This is due to the fact that at each scale one requires to solve for different boundary value problems simultaneously. An alternative to the costly FE^2 method is to incorporate a simulation-data-driven machine learning (ML) model as a surrogate model to the microscale problem. The surrogate model will describe the microscopic material behavior based on the macroscale variables and the microscopic properties. In this approach, a ML model will replace the microscale finite element problem at each integration point of the macroscopic finite element problem. Multiscale modeling using ML surrogates in the finite element simulations have been widely used in literature to describe the microscopic material behavior in macroscale simulations [38–42]. Readers are encouraged to see [43–45], for an overview on the state of the art of combining machine learning and multiscale modeling in various applications and pointed out available opportunities and challenges.

Ng et al. [46] provide an overview of emerging machine learning as a promising modeling approach to determine the state of charge and state of health of batteries. The authors also discussed the challenges such as modeling over different length scales and data generation. Petrich et al. [47] applied machine learning (ML) techniques for crack detection in lithium-ion cells. Jiang et al. [48] focused on the microstructure of a composite electrode. The authors combined multiscale experimental approaches, machine-learning-assisted statistical analysis, and experiment-informed mathematical modeling to understand the detachment of particles from the carbon/binder matrix. Hsu et al. [49] presented a ML approach to predict fracture processes. The data from the molecular simulation is fed into a deep learning network to have a physics-based data-driven multiscale model. Scharf et al. [50] presented opportunities for scale bridging utilizing nano-and microscale X-ray tomography and artificial intelligence in battery research. See also [51] for state-of-charge estimation of Li-ion batteries based on multichannel convolutional and bidirectional recurrent neural networks. Bao et al. [52] developed a machine learning coupled multiscale modeling for redox flow batteries. The authors also compared and validated the obtained information from the deep neural network against the experimental measurements. Teichert et al. [53] presented a scale bridging method that incorporates statistical mechanics methods with deep neural networks, and results in energies for specific atomic configurations. The resulting free energy functions from the lower scale made it possible to have atomistically informed phase-field simulations. Wen et al. [54] designed a physics-driven machine learning algorithm to map the temperature, stress, and rate-dependent deformation in Li-metal. The authors show the prediction capability of the model for the mechanical response of Li-metal. Later on, they integrated the trained network as a constitutive model in a finite element method.

As we employ the machine learning algorithm, it is also important to respect the underlying physics of the problem. Therefore, depending on the problem, additional (physical) constraints should be integrated within the network for more reliable predictions. Kohtz et al. [55] applied physics-informed machine learning model for an efficient estimation of battery state-of-health. See also [56], where authors developed a physically constrained image-learning framework to learn the chemo-mechanical constitutive law at the nanoscale from correlative scanning transmission electron microscopy images. It is also worth to mention the potential of the ML for the inverse design. Bhowmik et al. [57] presented a perspective for a future battery research in the direction of inverse design of battery interphases using multiscale modeling, experiments and generative deep learning. Nascimento et al. [58] presented a hybrid modeling by implementing physics within deep neural networks and showed that the hybrid battery model can be calibrated with a limited number of observations. Zhao et al. [59] employed a materials design strategy based on machine learning to design experimental conditions for the synthesis of lithium aluminum titanium phosphate as one potential solid electrolyte candidate. See also investigations by [60] on materials discovery to system optimization by integrating combinatorial electrochemistry and data science.

The main goal of the current work is to provide an efficient multiscale simulation method to study the battery cell performance by utilizing machine learning methods. Thereby we make use of the large chemo-mechanical simulation datasets at the microscale in solid-state batteries along with the interface delamination information. In Section 2.1, the governing equations and boundary conditions for both the macroscale and the microscale are summarized. Furthermore, the bridging between two scales is explained, and the proposed degradation function for the cell performance is discussed. In Section 2.2, a data-driven multiscale simulation framework for simulating the cell performance is provided. This framework is benchmarked against the concurrent multiscale method which already exists in the literature. In Section 3, the results are presented and explored where the new approach is used to capture the effect of the active material/solid electrolyte interface delamination on the cell performance. Finally, in Section 4 concluding remarks and opportunities for future developments are discussed.

2. Methods

2.1. Electro-chemo-mechanics of solid-state battery: two-level model formulation

The lithium battery cell configuration is shown in Fig. 1 at two different scales. Here, the battery cell contains a Li metal anode, a separator, and a composite cathode. The composite cathode consists of cathode active material and solid electrolyte. Anode and cathode current collectors, which are connected through the external circuit, are also attached to the anode and the cathode, respectively.

The two-level model formulation is based on the one presented in our previous work [31], but hereby not only active material but also solid electrolyte are resolved on the microscopic level. The kinetics and transport of lithium ions inside the electrolyte and the charge conservation are treated at the macroscale and the mechanically coupled transport of Li inside the cathode active material particles is treated at the microscale. Following the notation introduced by Doyle et al. [27], in this work's equations the subscript 1 refers to the cathode variables and 2 to the electrolyte variables. At the macroscale (cell level), the concentration of Li$^+$ in the solid electrolyte, c_2, the electric potential of the electrolyte phase, ϕ_2, and electric potential of the cathode (active material and the conducting agent combined), ϕ_1 are considered as system variables. The composite cathode is considered a homogenized phase containing cathode active material particles, carbon black, and the electrolyte. The degrees of freedom (DoFs) at the microscale used to describe the chemo-mechanically coupled model are the Li concentration in the cathode active material, c_1, and the displacement field, $\boldsymbol{u}$. The focus of this work is on the cathode side and its effect on the battery cell performance, and therefore only a half cell configuration is considered, but the framework and models are applicable to a full cell system as well. For the sake of completeness, the theoretical models are introduced for the two levels, respectively.

2.1.1. Electrochemical model at the macroscale

The mass balance for the specie i in the electrolyte is expressed via Nernst–Planck equation [61]:

$$\dot{c}_i = -\nabla \cdot \boldsymbol{J}_i = \nabla \cdot (D_i \nabla c_i) \ + \ \nabla \cdot (\frac{Z_i F D_i c_i}{RT} \nabla \phi_2). \tag{1}$$

According to the porous electrode theory, Eq. (1) is modified for the composite cathode [27] to account for the reaction between the electrolyte and the cathode active material. Therefore, a source term is added to the mass balance equation and effective transport properties are considered since the composite cathode is made of different phases. Modifying Eq. (1) and writing it for Li$^+$ results in:

$$\varepsilon_e \dot{c}_2 = \underbrace{\nabla \cdot (D_{\text{eff}} \nabla c_2)}_{\text{Diffusion}} \ + \ \underbrace{\nabla \cdot (\frac{F D_{\text{eff}} \ c_2}{RT} \nabla \phi_2)}_{\text{Migration}} \ + \ \underbrace{(1 - t_+^0) J_{\text{eff}}}_{\text{Reaction}}. \tag{2}$$

The first term in Eq. (2) is related to the flux of ions because of the diffusion and the second term considers the migration of Li$^+$ due to the electric field. The last term in the above equation is the source term, due to the electrochemical reaction (Eq. (3)).

$$\text{Li}^+ \ + \ \text{e}^- \longleftrightarrow \text{Li}. \tag{3}$$

The source term which is the macroscopic pore wall flux, J_{eff}, represents the amount of transferred ions resulting from the above electrochemical reaction. In Eq. (2), t_+^0 is the Li$^+$ transference number, which is the fraction of the current carried by the Li$^+$ over the whole current. In Eq. (2), ε_e is the volume fraction of the electrolyte phase in the composite cathode. Moreover, D_{eff} is the effective diffusivity in the composite cathode, which is the homogenized Li$^+$ diffusivity. It is calculated from the intrinsic diffusivity, $D_{2, \text{ intrinsic}}$, through Bruggeman homogenization relations [27]:

$$D_{\text{eff}} = D_{2, \text{ intrinsic}} \ \varepsilon_e^{1+\alpha}. \tag{4}$$
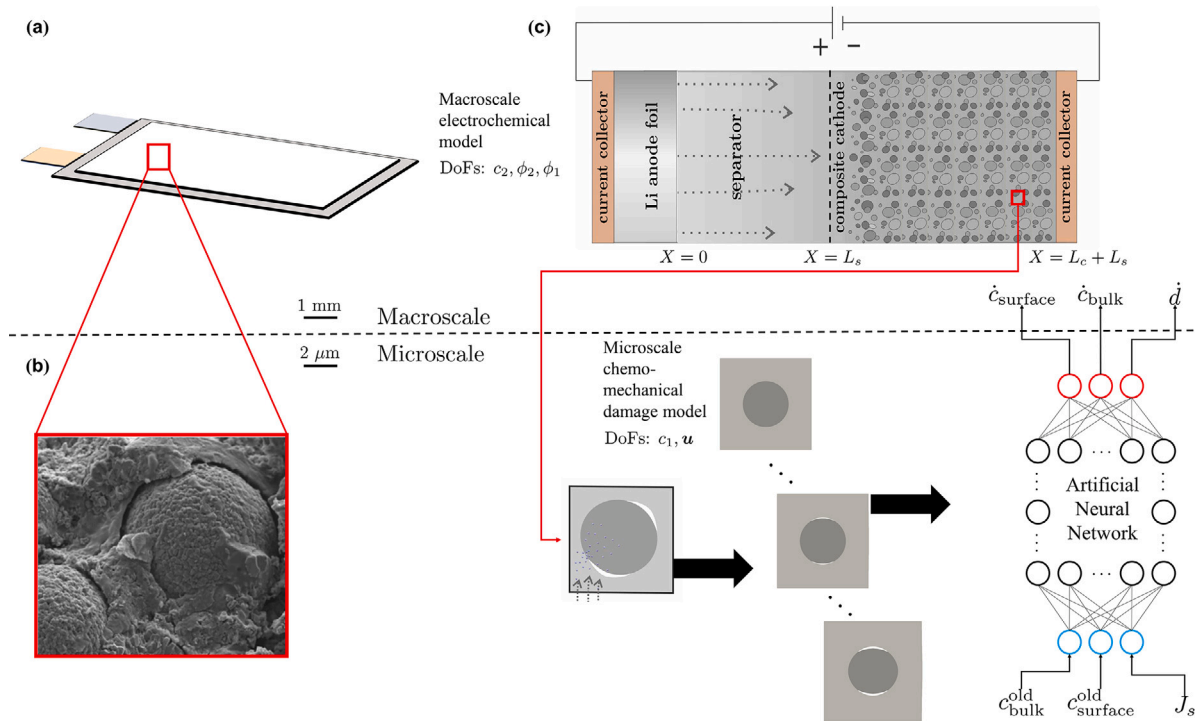
Fig. 1. Outline of the framework. (a) Lithium battery pouch cell, (b) SEM image of a possible microstructure of ASSB with the delamination between AM and SE, (c) the configuration of our simulation framework.
Source: The image in (b) is reprinted with permission from [4].
© 2017 American Chemical Society.

where α is the Bruggeman coefficient.

The focus of this work is on all-solid-state batteries. Some of the current promising solid electrolytes like lithium lanthanum zirconium oxide, $Li_7La_3Zr_2O_{12}$ (LLZO), are almost single ion conductors [62]. Experiments show that they have a transference number of $t_+^0 \approx 1$ for lithium ions [62], meaning that the anions in these materials are almost immobile. In this work the electrolyte is assumed to remain electroneutral, meaning $\sum_i c_i Z_i = 0$. Therefore using the same approach introduced by Wolff et al. [29], we assume that only cations, lithium ions, are mobile, and to fulfill the charge neutrality inside the electrolyte, the concentration of Li^+ should not change:

$$\dot{c}_2 = 0. \tag{5}$$

The effects of considering a constant Li^+ concentration in the electrolyte on the battery cell performance is already investigated by Wolff et al. [29]. The electrolyte current density, i_2 is associated with the summation of the flux of all charged species in the electrolyte [61] and is as follows:

$$i_2 = F \sum_i Z_i J_i. \tag{6}$$

Considering the flux, J_i, from the Nernst–Planck relation would yield:

$$i_2 = -F \sum_i Z_i D_i \nabla c_i - \kappa \nabla \phi_2, \tag{7}$$

where the electrolyte conductivity is defined as $\kappa = \frac{F^2}{RT} \sum_i D_i Z_i^2 c_i$. The above equation is a modified Ohm's law where the contribution of diffusion to electric current is taken into account. Considering a single ion conducting electrolyte affects Eq. (7) as well and it is rewritten as follows:

$$i_2 = -\kappa \nabla \phi_2. \tag{8}$$

Based on the porous electrode theory the effective conductivity, κ_{eff}, should be used in Eq. (8) instead of κ. Effective conductivity is calculated similarly to effective diffusivity through Bruggeman relations

[27]:

$$\kappa_{eff} = \kappa_{intrinsic} \, \varepsilon_e^{1+\alpha}. \tag{9}$$

In order to describe the current in the cathode phase, an Ohmic current is considered at the macroscale:

$$i_1 = -\sigma_{eff} \nabla \phi_1. \tag{10}$$

In Eq. (10), σ_{eff} is the effective electronic conductivity of the cathode, which is also calculated through Bruggeman relation [27] in Eq. (11)

$$\sigma_{eff} = \sigma_{intrinsic} \, \varepsilon_c^{1+\alpha}. \tag{11}$$

Here, ε_c is the volume fraction of the cathode phase in the composite cathode. The charge conservation at the macroscale for the electrolyte and the cathode is considered through Eqs. (12) and (13):

$$\nabla \cdot i_1 + F J_{eff} = 0. \tag{12}$$

$$\nabla \cdot i_2 - F J_{eff} = 0. \tag{13}$$

Similar to Eq. (2), the last term in the above equations which is a source term, represents the charge flux due to the charge transfer reaction between the electrolyte and the cathode active material. A summary of the electrochemical governing equations at the macroscale and their boundary conditions is presented in Table 1. Here we assume the galvanostatic charge/discharge process, where I is the applied current density to the cell (see also Fig. 1).

2.1.2. Chemo-mechanical model at the microscale

On the microscale two phases are regarded: a cathode active material particle inside a matrix of the solid electrolyte, as also illustrated in Fig. 1. The chemo-mechanically coupled transport of Li inside the active material at this scale is modeled using the model introduced in our previous work [11]. For this scale the Li concentration, c_1 (inside the active particle), and the displacement field, u (in both the solid electrolyte and the active material) are considered as DoFs. The governing equations for the balance of linear momentum and the balance of mass

Table 1
Electrochemical model at the macroscale.

Degree of freedom	Governing equation	Condition	Boundary
Electrolyte concentration, c_2	$\dot{c}_2 = 0$	$\boldsymbol{J}_{\mathrm{Li^+}} \cdot \boldsymbol{n} = 0$	$X = 0$
		$\boldsymbol{J}_{\mathrm{Li^+}} \cdot \boldsymbol{n} = 0$	$X = L_c + L_s$
Electrolyte potential, ϕ_2	$\nabla \cdot \boldsymbol{i}_2 - FJ_{\mathrm{eff}} = 0$	$\boldsymbol{i}_2 \cdot \boldsymbol{n} = -I$	$X = 0$
	$\boldsymbol{i}_2 = -\kappa_{\mathrm{eff}} \, \nabla \phi_2$	$\boldsymbol{i}_2 \cdot \boldsymbol{n} = 0$	$X = L_c + L_s$
Cathode potential, ϕ_1	$\nabla \cdot \boldsymbol{i}_1 + FJ_{\mathrm{eff}} = 0$	$\boldsymbol{i}_1 \cdot \boldsymbol{n} = 0$	$X = 0$
	$\boldsymbol{i}_1 = -\sigma_{\mathrm{eff}} \, \nabla \phi_1$	$\boldsymbol{i}_1 \cdot \boldsymbol{n} = I$	$X = L_c + L_s$

are introduced in Eqs. (18) and (19). Lithiation and delithiation cause expansion and shrinkage in the active material. Therefore, the strain in the active material is decomposed into the elastic, ϵ_e, and the chemical eigen-strain, ϵ_c:

$$\boldsymbol{\epsilon} = \frac{1}{2}(\nabla \boldsymbol{u} + \nabla \boldsymbol{u}^T) = \boldsymbol{\epsilon}_e + \boldsymbol{\epsilon}_c, \tag{14}$$

$$\boldsymbol{\epsilon}_c = (c - c_0) \, \boldsymbol{\Omega}, \quad \boldsymbol{\Omega} = \Omega_{ij} \, \boldsymbol{e}_i \otimes \boldsymbol{e}_j. \tag{15}$$

The chemical eigen-strain is related to the partial molar volume of the active material, Ω, this eigen-strain in NMC is highly anisotropic [17]. Therefore, following the work of Xu et al. [17], the tensor $\boldsymbol{\Omega}$ in the active material is defined as follows:

$$\boldsymbol{\Omega} = \begin{bmatrix} 2 & 0 & 0 \\ 0 & 2 & 0 \\ 0 & 0 & -1 \end{bmatrix} \frac{\Omega}{3}. \tag{16}$$

Note that the chemical eigen-strain is considered to be zero inside the solid electrolyte. The Cauchy stress tensor is calculated using Eq. (17)

$$\boldsymbol{\sigma} = \mathbb{C} : (\boldsymbol{\epsilon} - \boldsymbol{\epsilon}_c) = \mathbb{C} : \boldsymbol{\epsilon}_e. \tag{17}$$

In the above equation, $\mathbb{C}$ is the stiffness tensor. Then the balance of linear momentum in the absence of body forces reads as:

$$\nabla \cdot \boldsymbol{\sigma} = \boldsymbol{0}. \tag{18}$$

Finally, the mass balance for Li in the active material particle is expressed as:

$$\dot{c}_1 = \nabla \cdot \left[M_1 \nabla \left(RT \ln \frac{\tilde{c}_1}{1 - \tilde{c}_1} - \boldsymbol{\sigma} : \boldsymbol{\Omega} \right) \right]. \tag{19}$$

Here, $M_1 = \frac{D_1}{RT} c_1(1 - \tilde{c}_1)$ is the Li mobility in the cathode active material, and $\tilde{c}_1 = \frac{c_1}{c_{1,\max}}$ is the normalized Li concentration. The boundary condition for Eq. (19) is the microscopic pore wall flux (Eq. (26)) applied normal to the active particle surface. At the microscale this flux is only applied to the active particle. Further boundary conditions for the above governing equations are further exploited in the next section.

The cohesive zone model introduced in [11] is applied at the microscale to capture the delamination between the cathode active material particle and the solid electrolyte. Note that the cathode active material itself is considered as a homogenized median in this work without detailed internal interfaces, even though it is possible to include them theoretically and numerically [11]. Below a summary of equations used to calculate the mode-independent damage and the traction at the interface between active material and solid electrolyte is presented:

$$\Phi^d \leq 0, \tag{20}$$

$$d = \lambda \frac{\partial \Phi^d}{\partial Y}, \quad \dot{\xi} = -\lambda \frac{\partial \Phi^d}{\partial q_d}, \text{ KKT conditions,} \tag{21}$$

$$\boldsymbol{t}_I = f_d(d) \boldsymbol{R}^T \boldsymbol{K}_0 \, \boldsymbol{g}. \tag{22}$$

Here, $f_d = (1 - d)^n$ is the degradation function, Φ^d is the damage potential, Y is the damage driving force and q_d denotes the thermodynamically conjugate force for damage hardening.

$$Y = -\frac{1}{2} \frac{\mathrm{d} f_d(d)}{\mathrm{d} d} \, \boldsymbol{g}^T \boldsymbol{K}_0 \boldsymbol{g}, \tag{23}$$

$$q_d = H\xi, \tag{24}$$

$$\Phi^d = Y - (Y_0 + q_d). \tag{25}$$

In the above equations, Y_0 is the damage initiation energy, d is the damage variable, ξ is the damage hardening variable, H is the damage hardening parameter. Moreover, $\boldsymbol{g}$ is the interface gap vector, $\boldsymbol{K}_0$ is the initial interface stiffness and $\boldsymbol{R}$ is the rotation matrix. For further information and details about this model, readers are referred to our previous work [11].

The concentration and the electric potential of the electrolyte are assumed to be constant at the microscale and the governing equations related to them are solved at the macroscale. This assumption is because of the smaller size of the active material particle in comparison to the cell. Therefore, the only DoF considered in the solid electrolyte phase at the microscale is $\boldsymbol{u}$. The goal of having a matrix of solid electrolyte around the active particle at the microscale is (1) to capture the effect of the solid electrolyte and its mechanical properties on the deformation and the diffusion in the active material and (2) to model the interface delamination between the solid electrolyte and the active material.

2.1.3. Pore wall flux and bridging between scales

The reaction takes place at the interface between the electrolyte and the cathode active material, Eq. (3), and results in a flux which is described employing the Butler–Volmer relation in Eq. (26) [27]. The pore wall flux serves as the connection between the macroscale and the microscale. The effective macroscale pore wall flux, J_{eff} is used as a source term in the macroscale mass and charge balance equations (Eqs. (2), (12), (13)), and the microscale pore wall flux, J_s, is used as the boundary condition for the mass balance equation inside the active material (Eq. (19)). The microscopic pore wall flux is calculated as follows:

$$J_s = \frac{i_0}{F} \left[\bar{c}_{1,\,\mathrm{surface}} \exp\left(\frac{F\eta}{2RT} \right) - (1 - \bar{c}_{1,\,\mathrm{surface}}) \exp\left(\frac{-F\eta}{2RT} \right) \right]. \tag{26}$$

In Eq. (26), i_0 and η are the exchange current density and the overpotential, respectively. Here $\bar{c}_{1,\,\mathrm{surface}}$ is the average surface concentration of the cathode active material. They are calculated as:

$$i_0 = F k_2 \sqrt{(c_{2,\,\max} - c_2)c_2}, \tag{27}$$

$$\eta = \phi_1 - \phi_2 - U(c_{1,\,\mathrm{surface}}), \tag{28}$$

$$\bar{c}_{1,\,\mathrm{surface}} = \frac{\int_s c_1 \, dA}{\int_s dA}. \tag{29}$$

Here, k_2 is the reaction rate constant, and $c_{2,\,\max}$ is the maximum electrolyte concentration. The term $U(c_{1,\,\mathrm{surface}})$ is the open circuit potential of the cathode with respect to Li anode as a function of the cathode concentration. Here we utilized a function for $U(c_{1,\,\mathrm{surface}})$ which corresponds to lithium nickel manganese cobalt oxides, $\mathrm{LiNi}_x\mathrm{Mn}_y\mathrm{Co}_z\mathrm{O}_2$ (NMC). This function describes a fitted curve to experimental measurements [63] which reads:

$$U(c_{1,\,\mathrm{surface}}) = 7.9760 - 5.5419 \, c_{1,\,\mathrm{surface}} + 5.2824(c_{1,\,\mathrm{surface}})^{1.0700}$$
$$- 1.0556 \times 10^{-4} \exp(124.7407 \, c_{1,\,\mathrm{surface}} - 114.2593)$$
$$- 4.40446(c_{1,\,\mathrm{surface}})^{0.0766}. \tag{30}$$

Since the particle size is very small comparing to the cell length, the macroscale DoFs (c_2, ϕ_2, ϕ_1) at each point are considered to be constant at the microscale problem corresponding to that point. Therefore, a uniform ion flux is considered at the surface of the particles. This is also the reason for using $\bar{c}_{1,\,\mathrm{surface}}$ to calculate J_s in Eq. (26). The macroscopic pore wall flux is calculated from the microscopic pore wall flux, using Eq. (31).

$$J_{\mathrm{eff}} = a J_s. \tag{31}$$

Here, a is the specific interfacial area and denotes the surface area of the active material particles per volume of the composite cathode. This specific area is calculated as follows [31]:

$$a = \frac{S}{V} (1 - \varepsilon_e)(1 - \langle d \rangle). \tag{32}$$

In the above equation, S is the active material surface area in contact with the electrolyte, and V is the volume of the active material. Here $\langle d \rangle$ is the accumulative damage at the interface between the active material and the solid electrolyte. The accumulative damage is defined in Eq. (33) as the integral of the damage variable at the interface divided by the interface area.

$$\langle d \rangle = \frac{\int_s d \, dA}{\int_s dA}. \tag{33}$$

Delamination at the interface of cathode active material and the solid electrolyte is one major microscale mechanism. Upon lithiation and delithiation, the active material swells and shrinks in response to the changes in Li concentration. This results in a strain mismatch at the interface of the active material and the solid electrolyte, which causes interfacial damage and delamination. To account for the effect of this damage on cell performance, the degradation of the specific interfacial area in Eq. (32) is considered.

In this degradation relation, it is assumed that the delamination at the interface decreases the active interfacial area between the active material and the solid electrolyte. Meaning that the loss of contact between the active material and the solid electrolyte is considered to be the same as $\langle d \rangle$. In the limit case when $\langle d \rangle = 1$, the whole interface is damaged and the active particle becomes isolated. In the following section the sequential data-driven multiscale method to simulate the cell performance is discussed.

2.2. Data-driven multiscale framework

Machine learning methods have the potential to bypass the costly computations from the previous FE^2 methodology. To do so, the idea is first to perform large numbers of offline simulations at the microscale by varying important features within the desired range. Next, by utilizing machine learning algorithms one can train a model based on these data. The machine learning method used in this work is an artificial neural network (ANN). The flowchart of the ANN-assisted multiscale method is given in Fig. 2. In this figure, the macroscale steps are shown in blue, and the steps which predict the microscale response are drawn in red.

Here at an arbitrary time t^i, first the effective pore wall flux, J_{eff}, is calculated using Eqs. (26)–(33). Then the macroscale equations (Table 1) are solved and the macroscale DoFs for time t^{i+1} are updated. Simultaneously, the microscopic pore wall flux is calculated from Eq. (26). Then this value along with the current active material average surface and bulk concentrations, namely $\bar{c}^i_{1,\text{ surface}}$ and $\bar{c}^i_{1,\text{ bulk}}$ is used as inputs for the surrogate model. Next the surrogate model outputs the $\dot{\bar{c}}^i_{1,\text{ surface}}$, $\dot{\bar{c}}^i_{1,\text{ bulk}}$ and $\langle \dot{d} \rangle^i$. The first two outputs are the current increments of average surface and bulk concentrations over time, and the last output is the change in the accumulative damage at the interface of the active material and the solid electrolyte with respect to time. Next, using Eqs. (34) and (36) the updated values of the active material average surface and bulk concentrations and the accumulative damage ($\bar{c}^{i+1}_{1,\text{ surface}}$, $\bar{c}^{i+1}_{1,\text{ bulk}}$ and $\langle d \rangle^{i+1}$) are calculated. Finally the active material properties are updated and the next time step starts, and the sequence keeps repeating. Eqs. (34)–(36) show the relations used to obtain the new active material properties from their increments. Here, Δt is the time step size and is defined as $\Delta t = t^{i+1} - t^i$.

$$\bar{c}^{i+1}_{1,\text{ surface}} = \bar{c}^i_{1,\text{ surface}} + \dot{\bar{c}}^i_{1,\text{ surface}} \, \Delta t, \tag{34}$$

$$\bar{c}^{i+1}_{1,\text{ bulk}} = \bar{c}^i_{1,\text{ bulk}} + \dot{\bar{c}}^i_{1,\text{ bulk}} \, \Delta t, \tag{35}$$

$$\langle d \rangle^{i+1} = \langle d \rangle^i + \langle \dot{d} \rangle^i \, \Delta t. \tag{36}$$

2.2.1. Training data

In order to calibrate and test the surrogate model, proper data sets should be generated, which is done by performing finite element simulations on the microscale problem. Here the boundary condition for balance of mass equation is the microscopic pore wall flux. The displacement boundary condition depends on the specific study and will be mentioned later in the related study. The value of pore wall flux depends on the cell parameters and more importantly on the applied current density, I. A range of values for J_s which may occur during the process is obtained by running a FE^2 simulation on a specific macroscale configuration and parameters. Next, using several J_s values from this range, individual microscale simulations are performed (for each simulation a constant J_s is used). Considering one of these simulations, values for $\bar{c}_{1,\text{ surface}}$, $\bar{c}_{1,\text{ bulk}}$, Δt and $\langle d \rangle$ are stored for each time step. Then using a post processing, for each time step, values of $\dot{\bar{c}}^i_{1,\text{ surface}}$, $\dot{\bar{c}}^i_{1,\text{ bulk}}$ and $\langle \dot{d} \rangle^i$ are calculated. These relations are presented below, where $i = 0, 1, 2, \ldots, n$, and n is the number of time steps:

$$\dot{\bar{c}}^i_{1,\text{ surface}} = (\bar{c}^{i+1}_{1,\text{ surface}} - \bar{c}^i_{1,\text{ surface}}) \frac{1}{\Delta t}. \tag{37}$$

$$\dot{\bar{c}}^i_{1,\text{ bulk}} = (\bar{c}^{i+1}_{1,\text{ bulk}} - \bar{c}^i_{1,\text{ bulk}}) \frac{1}{\Delta t}. \tag{38}$$

$$\langle \dot{d} \rangle^i = (\langle d \rangle^{i+1} - \langle d \rangle^i) \frac{1}{\Delta t}. \tag{39}$$

A set including $\{J_s, \bar{c}^i_{1,\text{ surface}}, \bar{c}^i_{1,\text{ bulk}}, \dot{\bar{c}}^i_{1,\text{ surface}}, \dot{\bar{c}}^i_{1,\text{ bulk}}, \langle \dot{d} \rangle^i\}$ is saved for each time step of the simulation. For the sake of simplicity, this set is presented as $\{J_s, c^{\text{old}}_{\text{surface}}, c^{\text{old}}_{\text{bulk}}, \dot{c}_{\text{surface}}, \dot{c}_{\text{bulk}}, \dot{d}\}$. By changing J_s and running further microscale simulations and then repeating the steps discussed above, data sets containing different J_s values are generated. Putting all of these data sets together, creates the data required for developing the surrogate model.

2.2.2. Surrogate model formulation

A feedforward neural network (FFNN) is used to obtain the surrogate model which represents the microscale material response. The input of the model in the vector (array more exactly) form will be $\boldsymbol{In} = (J_s, c^{\text{old}}_{\text{surface}}, c^{\text{old}}_{\text{bulk}}) \in \mathbb{R}^3$. The output of the model in the vector form is $\boldsymbol{Out} = (\dot{c}_{\text{surface}}, \dot{c}_{\text{bulk}}, \dot{d}) \in \mathbb{R}^3$, this vector is a function of inputs, meaning $\boldsymbol{Out}(\boldsymbol{In})$. Hence a surrogate model $\hat{\boldsymbol{M}}(\boldsymbol{In}) : \mathbb{R}^3 \to \mathbb{R}^3$ is developed using FFNNs which satisfies $\hat{\boldsymbol{M}}(\boldsymbol{In}) \equiv \boldsymbol{Out}(\boldsymbol{In})$. Fig. 3 shows a schematic structure of a neural network model. The network consists of an input layer, N hidden layers and an output layer. Each layer is denoted by $\boldsymbol{Z}^i$. Each layer consists of several nodes which are expressed by z^i_j, which means the jth node of the ith layer.

The input layer consists of the scaled values of the physical inputs ($\boldsymbol{In}$) and has 3 nodes, namely $\boldsymbol{Z}^0 = \boldsymbol{Sc}(\boldsymbol{In}) \in \mathbb{R}^3$, where $\boldsymbol{Sc}$ is the input scaling function. The values of the nodes in hidden layers and the output layer are calculated using Eq. (40). There $\boldsymbol{Z}^i \in \mathbb{R}^n$ (for $i = 1, 2, \ldots, N$ and n is the number of nodes in the layer i), and $\boldsymbol{Z}^{N+1} \in \mathbb{R}^3$.

$$\boldsymbol{Z}^i = a^i(\boldsymbol{W}^i \boldsymbol{Z}^{i-1} + \boldsymbol{b}^i) \ , \quad i = 1, 2, \ldots, N + 1. \tag{40}$$

In Eq. (40), $\boldsymbol{W}^i \in \mathbb{R}^{n^i \times n^{i-1}}$, $i = 1, 2, \ldots, N + 1$ is the weights matrix for the ith layer with n^i being the number of nodes in that layer, $\boldsymbol{b}^i \in \mathbb{R}^{n^i}$, $i = 1, 2, \ldots, N + 1$ is the biases associated with each layer, and a^i , $i = 1, 2, \ldots, N + 1$ represents the activation function. The final output of the surrogate model is obtained from scaling back the output layer, meaning $\hat{\boldsymbol{M}}(\boldsymbol{In}) = \boldsymbol{Bsc}(\boldsymbol{Z}^{N+1})$. Thereby $\boldsymbol{Bsc}$ is the output back scaling function.

In order to determine the surrogate model, the number of hidden layers and their nodes, and the activation functions are set. Then the weights and the biases are determined. This determination is done by minimizing an objective function which is defined in Eq. (41). The data generated from microscale simulations is split into 2 groups: the training group ($\boldsymbol{T}^{\text{in}}, \boldsymbol{T}^{\text{out}}$) and the test group ($\boldsymbol{P}^{\text{in}}, \boldsymbol{P}^{\text{out}}$). The objective
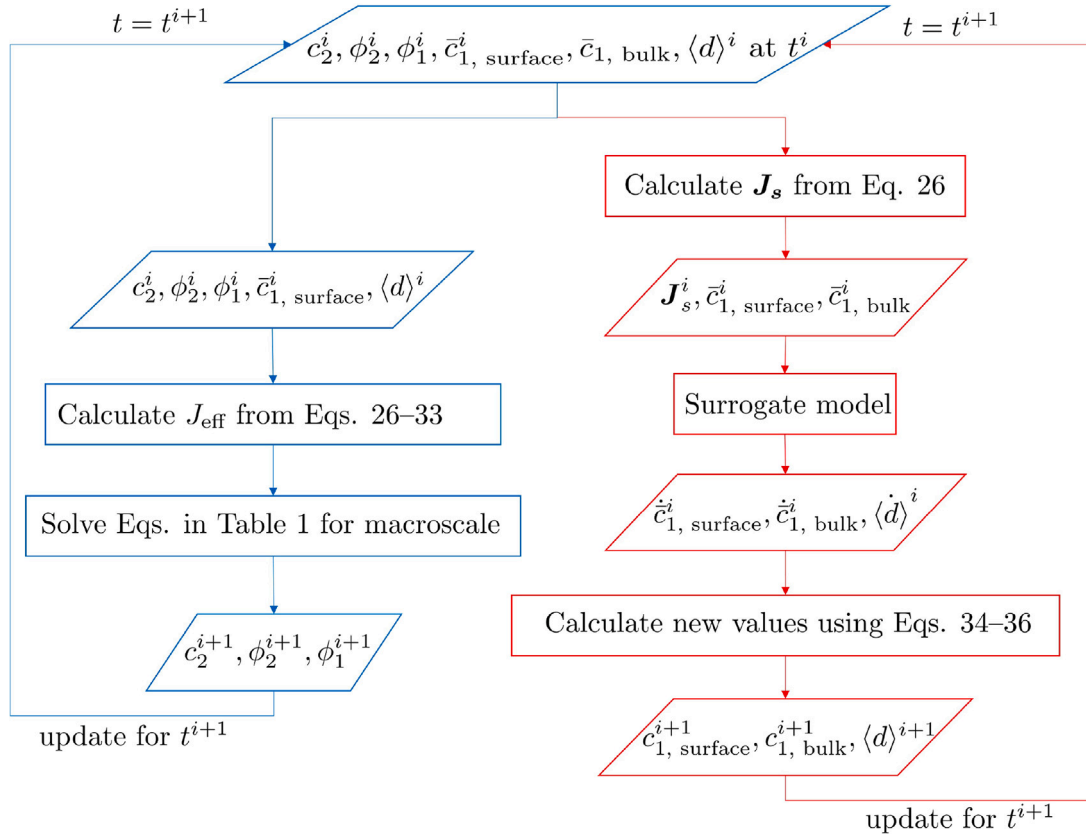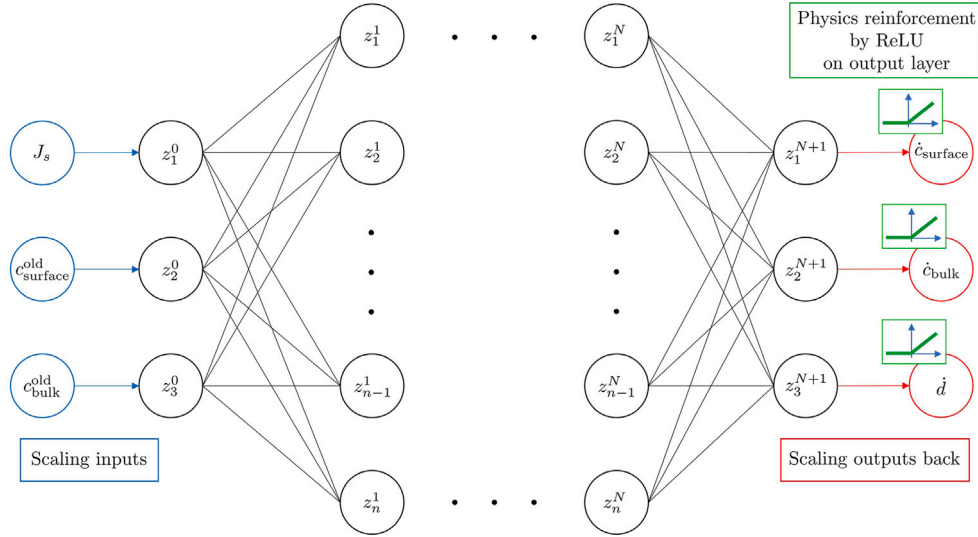
Fig. 2. Flowchart of the ANN-assisted multiscale method.

Fig. 3. Structure of an ANN with N hidden layers and n nodes in each hidden layer.

function is minimized for the training data set. The test sets will not be exposed to the model until the model has been trained.

$$E(\boldsymbol{T}^{\text{in}}) = \frac{1}{3}\sum_{i=1}^{3}\frac{1}{n_{\boldsymbol{T}^{\text{in}}}}\sum_{\boldsymbol{T}^{\text{in}}}\left[\hat{\boldsymbol{M}}_i(\boldsymbol{T}^{\text{in}}) - \boldsymbol{T}_i^{\text{out}}(\boldsymbol{T}^{\text{in}})\right]^2 + \lambda\sum_i\sum_j\sum_k(\boldsymbol{W}_{jk}^i)^2.$$

(41)

To interpret the output of the network and to ensure fulfillment of the physics (i.e. to have always non-negative values for damage growth) we have applied a ReLU activation function (see Eq. (48)) on

the last layer (please see Fig. 3). Usually, in the regression problem, there is no activation function on the output layer. Here, it is worth mentioning that the last layer activation function will not manipulate the data dramatically. Since ReLU is piecewise linear and can cover the whole range of values of the output, except the negative one. In other words, the purpose of adding non-linearities of ReLU in hidden layers is to add non-linear boundaries which can accept all possible positive choices, which fits perfectly the regression tasks here. ReLU is different compared to the other non-linear activation function like softmax, which limits the choice of outputs by making certain upper and lower boundaries. In this method, the learning which is nothing

more than the optimization of bias and weight is done in presence of this last layer ReLU. Therefore, the employed approach to fulfill the physics of the problem is different from the other constrained ANN, which impose a penalty on the loss function [64]. It is interesting to also examine such strategies in future studies.

The first term in Eq. (41) is the mean squared error (MSE). The MSE is calculated for each component of the output vector and then averaged over them. Here $n_{T_{in}}$ is the number of samples in data set. The last term in Eq. (41) is the L2 regularization term which helps to avoid overfitting. Here λ is a non-negative hyperparameter and controls the contribution of the regularization term. In Eq. (41), W^i_{jk} is a component of the weights matrix of the layer i, which is in the jth row and the kth column of the matrix.

After determining the surrogate model, the test sets are used to evaluate the model's performance. In this work MSE and the coefficient of determination, R^2 are used for this purpose. The former is explained in the above paragraph, and the latter, R^2, for the test set is defined as follows:

$$R^2(\boldsymbol{P}^{\text{in}}) = \frac{1}{3} \sum_{i=1}^{3} \left[1 - \frac{\sum_{\boldsymbol{P}^{\text{in}}} [\hat{\boldsymbol{M}}_i(\boldsymbol{P}^{\text{in}}) - \boldsymbol{P}_i^{\text{out}}(\boldsymbol{P}^{\text{in}})]^2}{\sum_{\boldsymbol{P}^{\text{in}}} [\boldsymbol{P}_i^{\text{out}}(\boldsymbol{P}^{\text{in}}) - \bar{\boldsymbol{P}}_i^{\text{out}}(\boldsymbol{P}^{\text{in}})]^2} \right] \tag{42}$$

where, $\bar{\boldsymbol{P}}_i^{\text{out}}(\boldsymbol{P}^{\text{in}})$ is the average of the component i of the physical outputs and is defined as $\bar{\boldsymbol{P}}_i^{\text{out}}(\boldsymbol{P}^{\text{in}}) = \frac{1}{n_{\boldsymbol{P}^{\text{in}}}} \sum_{\boldsymbol{P}^{\text{in}}} \boldsymbol{P}_i^{\text{out}}(\boldsymbol{P}^{\text{in}})$, where $n_{\boldsymbol{P}^{\text{in}}}$ is the number of samples in test data set.

Remark. The inputs and the outputs used for the surrogate model are the system variables necessary for solving the equations. Microscale material properties (such as fracture properties, active material diffusivity, ...) can also be considered as inputs to the surrogate model, which also requires proper data generation by varying the desired property. Adding fracture energy (G_c) as one of the inputs is investigated in Section 3.2.

2.2.3. Implementation aspects

The training data is obtained from the finite element simulations on the microscopic level using the open-source framework "Multiphysics Object-Oriented Simulation Environment" (MOOSE) [65]. Through a post-processing step, the input data for the ANN training are obtained. The calculations related to the machine learning part are performed in python 3.8.8 and by using the Keras packages [66] and employing scikit-learn [67] for some of the pre-processing steps. Next, the obtained ML model is exported in terms of its weights and biases as numbers in a text file, which is then used in the MOOSE input file for the multiscale simulation. The ANN is built using the weights, biases and activation function in a subroutine in MOOSE in C++ programming language using simple arithmetic operations. During the multiscale simulation, the neural network is called and evaluated at each integration point and each iteration of the macroscopic simulation.

3. Results and discussion

Before we demonstrate data-driven simulation results for solid-state batteries, the data-driven multiscale framework is first benchmarked against the FE^2 two-level framework [31] for the case of conventional Li-ion battery. The parameters used in the simulations of this section are listed in Tables 2 and 3. These parameters are related to LLZO for the solid electrolyte and NMC for the cathode active material.

3.1. Benchmark

In order to benchmark the data-driven method against the FE^2 method, identical simulation setup and parameters are used for both of them. Since the FE^2 method has a high computation cost, just simple

Table 2
Parameters used in the microscale simulations, taken from [17,68–70].

Parameters for the model at the microscale		
	Unit	Value
Young's modulus of cathode E_1	[GPa]	140.0
Maximum Concentration of cathode $c_{1, \text{max}}$	[mol/m^3]	38320
Poisson's ratio of cathode v_1	[–]	0.3
Cathode partial molar volume Ω	[m^3/mol]	4.566×10^{-6}
Cathode diffusivity D_1	[m^2/s]	7×10^{-15}
Damage initiation energy Y_0	[Pa m]	0.977, 1.47, 2.86
Damage hardening parameter H	[Pa m]	5.294, 7.33, 18.165
Interface stiffness k_0	[Pa/m]	3.26×10^{16}
Gas constant R	[J/(mol K)]	8.314
Temperature T	[K]	298.15

Table 3
Parameters used in the macroscale simulations, taken from [27,71–73].

Parameters for the model at the macroscale		
	Unit	Value
Young's modulus of electrolyte E_2	[GPa]	150
Maximum concentration of electrolyte $c_{2, \text{max}}$	[mol/m^3]	5433
Initial concentration of electrolyte c_2^0	[mol/m^3]	1200
Poisson's ratio of electrolyte v_2	[–]	0.2
Electrolyte conductivity $\kappa_{\text{intrinsic}}$	[S/m]	2.44×10^{-2}
Cathode electronic conductivity $\sigma_{\text{intrinsic}}$	[S/m]	10
Reaction rate constant k_2	[m^4/(mol s)]	10^{-10}
Spring constant K_{spring}	[N/m]	8.15×10^4
Volume fraction of the electrolyte ε_e	[–]	0.3
Volume fraction of the cathode conductive phase ε_c	[–]	0.3

Fickian diffusion (Eq. (43)) is used as the governing equation at the microscale. Meaning that the only DoF at the particle level is c_1.

$$\dot{c}_1 = \nabla \cdot (D_1 \nabla c_1). \tag{43}$$

Since mechanical coupling is not considered in this subsection, there is no need to model the electrolyte phase at the microscale. Therefore, the microscale in this study consists of just a spherical active material particle. Fig. 4(a) shows the particle schematically. Another simplification for the microscale model is done by considering only radial diffusion in the active material. The diffusion equation in spherical coordinate system (only radial) is presented in Eq. (44). The microscale problem is now a one dimensional diffusion in the direction of radius.

$$\dot{c}_1 = \frac{1}{r^2} \frac{\partial}{\partial r} \left(D_1 r^2 \frac{\partial c_1}{\partial r} \right). \tag{44}$$

In the above equation, r is the radial coordinate. The boundary conditions for the above equation are as follows (R_s is the radius of active particle):

$$\frac{\partial c_1}{\partial r} = J_s \quad \text{at } r = R_s, \tag{45}$$

$$\frac{\partial c_1}{\partial r} = 0 \quad \text{at } r = 0. \tag{46}$$

Macroscale equations are the ones presented in Table 1. Parameters used in this study are also given in Tables 2 and 3. The 1D battery cell consists of a separator with the length of $L_s = 40$ μm and a composite cathode which is $L_c = 60$ μm long. The radius of the active material particle is also $R_s = 1$ μm. The applied current density to perform the galvanostatic discharging is $I = 11.7$ A/m^2. This current corresponds to the C-rate of 1. In this work the concentration range for cathode active material is considered to be $(0.5 - 1) c_{1, \text{max}}$, therefore the initial active material concentration is set to $0.5 c_{1, \text{max}}$.

Fig. 4(b) shows the cell potential with respect to time for the FE^2 simulation with different time step sizes, dt. The multiscale problem is solved using a staggered approach, meaning that microscale variables are treated as constants at the macroscale and vice versa. Therefore, the time step size should be small enough to have an accurate solution.
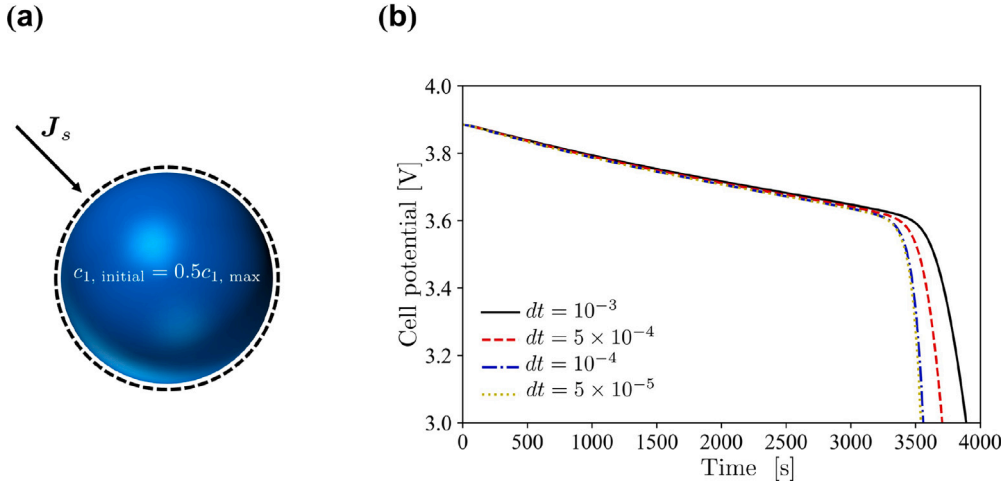
Fig. 4. (a) Schematic illustration of the microscale, and (b) cell performance results from the FE^2 simulation.

Table 4
Performance of the surrogate model used in benchmarking.

$R^2(\boldsymbol{P}^{\text{in}})$	MSE($\boldsymbol{P}^{\text{in}}$)
0.9979	0.0001

Fig. 4(b) shows that the solution converges by decreasing dt. The result with time step size $dt = 5 \times 10^{-5}$ is chosen as the solution.

Data required to train and test the surrogate model is generated by running simulations with constant flux boundary condition applied to a spherical active material particle. The applied flux boundary condition should be in the range of J_s values which occur during the macroscale simulation. An evaluation of this range is made from the FE^2 simulation results. For this case $J_s \in [2.8 \times 10^{-7}, 2.6 \times 10^3]$ mol/(m^2 s). For each simulation with n time steps, n data sets in the form of $\{J_s, c_{\text{surface}}^{\text{old}}, c_{\text{bulk}}^{\text{old}}, \dot{c}_{\text{surface}}, \dot{c}_{\text{bulk}}\}$ are generated. Since this is a pure electrochemical study and contains no mechanics, damage is not among the outputs of the surrogate model. Overall around 6000 data sets of this form are produced. A surrogate model is trained and tested using these data. This model, which is an ANN has 1 hidden layer with 704 nodes.

Scaling of both the input and the output data is done through min–max scaling. The scaling equation used for an arbitrary variable x is as follows:

$$\tilde{x} = \frac{x - \min(x)}{\max(x) - \min(x)}. \tag{47}$$

Here $\tilde{x}$ is the scaled value for x, and $\min(x)$ and $\max(x)$ represent the minimum and the maximum values of the variables in the data set respectively. The input J_s is scaled with an extra step: The min–max scaling is done on the $\log_{10}(J_s)$. The reason for this is the distribution of J_s, i.e. for each simulation, J_s is chosen as $J_s = m \times 10^n$ with $m \in [1, 9]$ and $n = -7, -6, \ldots, 3$. By taking $\log_{10}(J_s)$, the input is redistributed more uniformly. Moreover, the ReLU is used as the activation function, which is defined as:

$$a^i(\boldsymbol{Z}^i) = \max(0, \boldsymbol{Z}^i). \tag{48}$$

Here, the outputs of the ANN are also treated with a ReLU activation function. It ensures that our outputs, $\{\dot{c}_{\text{surface}}, \dot{c}_{\text{bulk}}\}$, are always non-zero, which is a physical necessity in our problem. The R^2 score and the MSE of this model for the test sets are presented in Table 4 below.

Next the surrogate model is implemented in a macroscale finite element simulation to describe the microscale behavior (see the flowchart in Fig. 2). The evolution of the cell potential for this simulation along with the FE^2 result ($dt = 5 \times 10^{-5}$) are presented in Fig. 5(a). The

results of the data-driven method are in acceptable agreement with those obtained from the FE^2 method.

The evolution of the $\bar{c}_{1,\text{surface}}$ with respect to time for these two methods is also plotted in Fig. 5(b). In terms of computation cost, the data-driven method has a significantly higher efficiency than the FE^2 method. It takes 4 days to run this problem using FE^2 method on a computer with 48 cores on Intel® Xeon® Platinum 9242 Processor, with 2x Intel® AVX-512 units per core, while it takes only 20 min to run it using the data-driven method on the same machine.

3.2. Data-driven multiscale simulation of chemo-mechanical behavior and damage of solid-state batteries

In this section the data-driven framework is used to evaluate the active material/solid electrolyte interface delamination and its effect on the cell performance during galvanostatic battery discharge.

3.2.1. Microscale simulations

The discretized geometry and the boundary conditions used at the microscale for this study are presented in Fig. 6.

In order to generate large amounts of training data and demonstrate the framework of data-driven strategy, we first examine a circular active material particle in a matrix of solid electrolyte. An extension to spherical particles is straightforward. The microscopic pore wall flux is applied as a constant flux to the active particle. The left boundary of the geometry is fixed in the x-direction ($u_x = 0|_{\text{left}}$). In order to avoid rigid body motion, the center of the active particle is fixed in the y-direction. The top and bottom boundaries have periodic displacement boundary condition, which is depicted in Fig. 6(b) for an arbitrary deformation. The right boundary has a spring boundary condition in the x-direction, where the associated force, F is calculated according to the equation below:

$$F = -K_{\text{spring}} \, u_x. \tag{49}$$

Here, K_{spring} is the spring constant. In this study, interface fracture energy, G_c, is also considered as one of the inputs of the surrogate model. Therefore, it will be possible to get different damage evolutions for battery cells with different interface fracture energies. This also means that G_c should be changed for the microscale simulations to have a proper training data. Three values are chosen for G_c, namely $G_c \in \{4.21, 5.97, 13.92\}$ J/m^2. The Y_0 and H values given in Table 2 are associated with these three fracture energies in the same order as mentioned above.

Microscale simulations are performed by applying constant J_s to the active particle. The applied J_s is chosen as $J_s \in [2.8 \times 10^{-7}, 8.3 \times 10^2]$
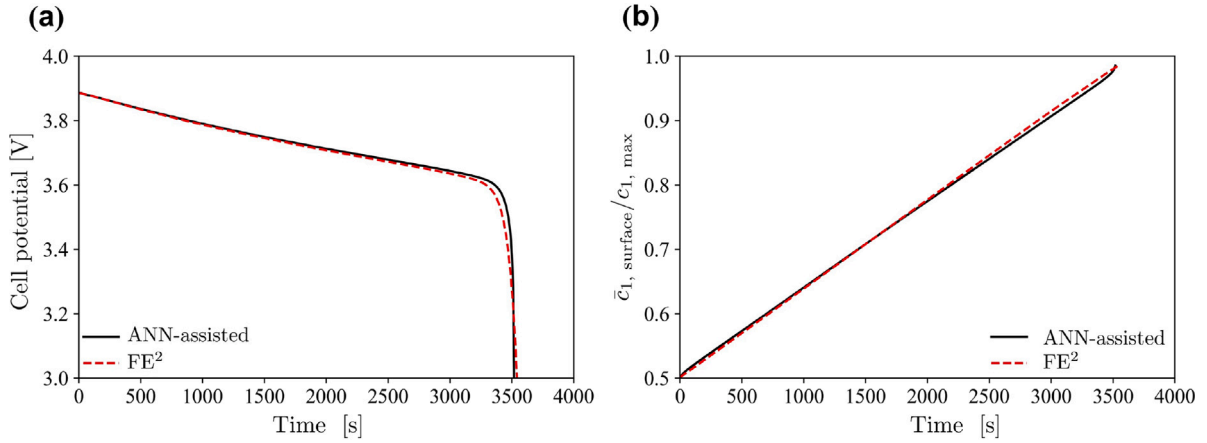
(a)

(b)

Fig. 5. Cell potential and surface concentration evolution for ANN-assisted and FE^2 frameworks.
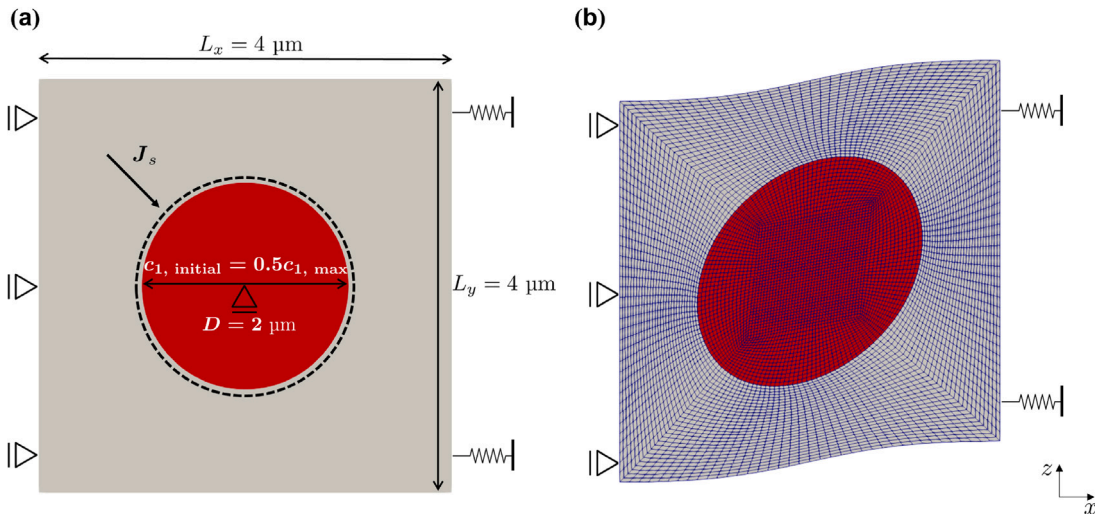
(a)

(b)

Fig. 6. Discretized geometry of the microscale problem and its boundary conditions.

mol/(m^2 s), for which the corresponding FE^2 simulations were carried out. Fig. 7 depicts the active material concentration and the damage at three instances during one of these microscale simulations as an example, where $G_c = 5.97$ J/m^2 and $J_s = 783$ mol/(m^2 s) are used. As seen in Fig. 7, during lithiation the concentration of the active material particle increases, which causes the particle to deform anisotropically, where it shrinks in the z direction and expands in the x direction. Since the Li flux inside the particle is influenced by the gradient of the stress (see Eq. (19)), this anisotropic deformation causes an also anisotropic diffusion front which is illustrated in concentration profiles in Fig. 7. Moreover, the lithiation causes both a normal and a shear gap at the areas shown in Fig. 7 at the interface of the active material and the solid electrolyte due to the anisotropy of the induced deformation. Similar to the previous study, for each time step of each simulation, data sets consisting of $\{G_c, J_s, c_{\text{surface}}^{\text{old}}, c_{\text{bulk}}^{\text{old}}, \dot{c}_{\text{surface}}, \dot{c}_{\text{bulk}}, d\}$ are saved. Finally around 12304 data sets of this form are produced. The microscale simulations also show that in cases with smaller fracture energies the interface starts to delaminate sooner and the final damaged fraction of the interface is bigger.

3.2.2. Surrogate model including the delamination effects

The range of values considered for J_s is wide, which in turn results in a wide range of values for the output values (especially $\dot{c}_{\text{surface}}, \dot{c}_{\text{bulk}}$). Therefore, the data set acquired from the microscale simulations is divided into 3 subsets based on their value of J_s, and each subset is used to train an ANN, which together make the surrogate model. Each

Table 5
Performance of the chemo-mechanically coupled surrogate model.

$R_1^2(\boldsymbol{P}^{\text{in}})$	$R_2^2(\boldsymbol{P}^{\text{in}})$	$R_3^2(\boldsymbol{P}^{\text{in}})$	MSE$_1(\boldsymbol{P}^{\text{in}})$	MSE$_2(\boldsymbol{P}^{\text{in}})$	MSE$_3(\boldsymbol{P}^{\text{in}})$
0.99184	0.99556	0.99316	0.00001	0.00006	0.00006

of these networks has 1 hidden layer, the first one has 128 nodes and the other two networks have 2048 and 3072 nodes in their hidden layer, respectively. Scaling of both the input and the output data is done through min–max scaling, and ReLU is used as the activation function. Similar to the previous section and for the same reason, J_s is scaled in two steps, meaning that $\log_{10}(J_s)$ is used for min–max scaling. In this model, the outputs of the ANN are treated with a ReLU activation function as well to ensure non-zero outputs, $\dot{c}_{\text{surface}}, \dot{c}_{\text{bulk}}, d \geq 0$. The R^2 score and the MSE of the chemo-mechanically coupled surrogate model for the test sets of each neural network are presented in Table 5.

In order to test the prediction performance of the ML model with a fracture energy that it has not seen before, two microscale simulations with two unseen fracture energies are performed. In one case $G_c = 5$ J/m^2 is chosen and constant $J_s = 261$ mol/(m^2 s) is applied and in the second case $G_c = 10$ J/m^2 and $J_s = 183$ mol/(m^2 s) are used. These parameters are then used in the surrogate model to get the evolutions of $\bar{c}_{1, \text{surface}}, \bar{c}_{1, \text{bulk}}$ and accumulative damage ($\langle d \rangle$) with respect to time. Fig. 8 depicts the results for both the finite element simulations and the surrogate model predictions. The first row (sub-figures (a), (b) and
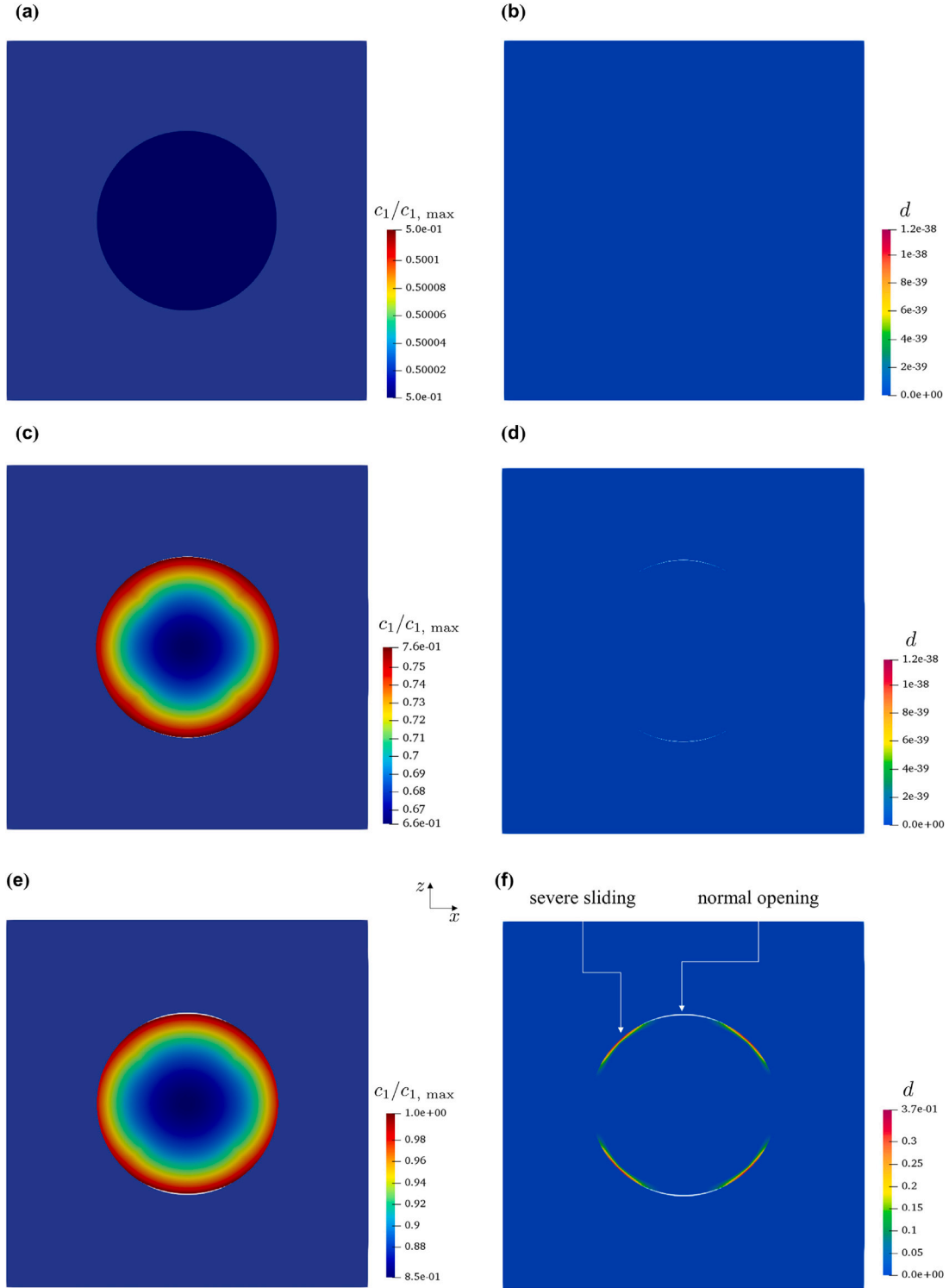
Fig. 7. AM concentration and damage at the beginning (a and b), the middle (c and d) and at the end (e and f) of the simulation with $G_c = 5.97$ J/m^2 and $J_s = 783$ mol/(m^2 s).

(c)) are related to the first case ($G_c = 5$ J/m^2, $J_s = 261$ mol/(m^2 s)) and the second row (sub-figures (d),(e) and (f)) shows the results for the second case ($G_c = 10$ J/m^2, $J_s = 183$ mol/(m^2 s)). As shown in Fig. 8, surrogate model predictions are in good agreement with the finite element simulation results even for unseen fracture energies.

3.2.3. Cell performance simulation

The developed surrogate model is used in the macroscale finite element simulation as explained in the flowchart presented in Fig. 2.

Similar to the previous study, the 1D battery cell consists of a separator and a composite cathode with the lengths of $L_s = 40$ μm and $L_c = 60$ μm, respectively. The applied discharge current density is $I = 11.7$ A/m^2 which corresponds to 1 C.

In the first study the damage evolution and its effect on the cell performance is investigated. The interfacial fracture energy of the active material/solid electrolyte interface is set to $G_c = 5.97$ J/m^2. Fig. 9 depicts the cell potential and the damage evolution with respect to time for this cell, the sub-figure (b) depicts the average damage value
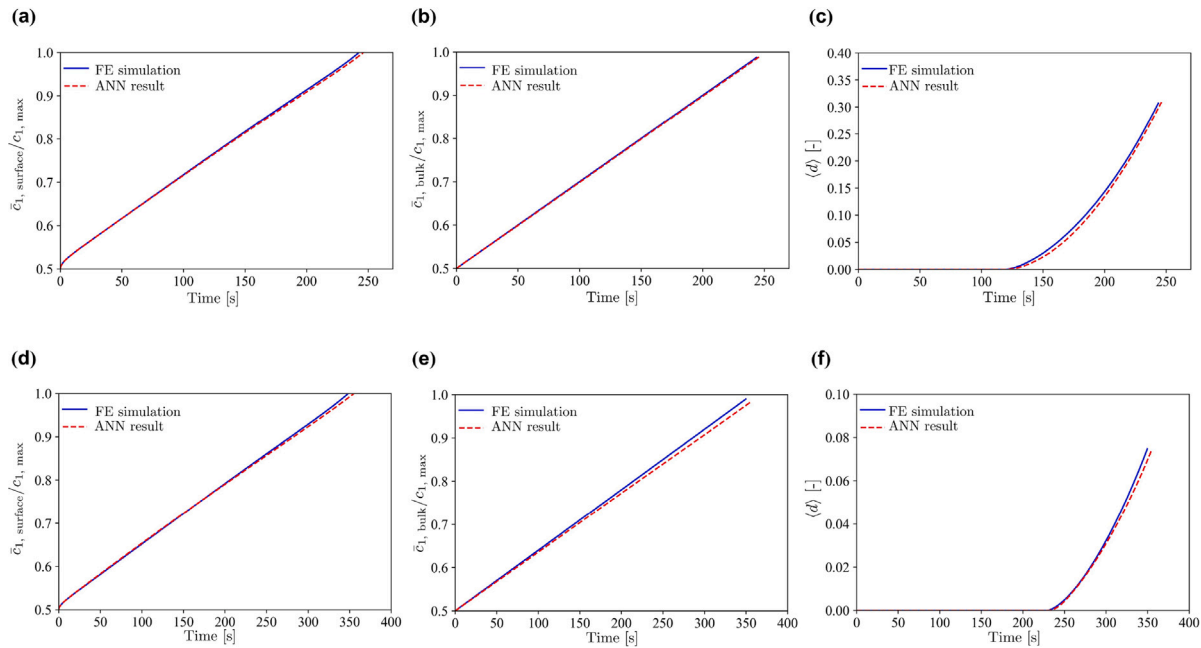
Fig. 8. Validation of the surrogate model predictions for unseen fracture energies: (a), (b) and (c) correspond to $G_c = 5$ J/m^2, $J_s = 261$ mol/(m^2 s). (d), (e) and (f) are related to $G_c = 10$ J/m^2, $J_s = 183$ mol/(m^2 s).

along the length of the composite cathode. Damage starts to evolve when the interface between the active material and the solid electrolyte in at least one of the particles undergoes delamination, results show that this first occurs to the particles of the composite cathode close to the separator.

As depicted in Fig. 9, the interface damage degrades the cell capacity. The blue curve in Fig. 9(b) is the cell performance without the consideration of the effect of the damage and the red curve shows the cell performance with the damage effect. As the damage evolves, the cell potential drops faster and the final delivered capacity becomes smaller. This can be explained by the degradation relation (Eq. (32)), which assumes that the active interface area between the active material and the solid electrolyte is reduced due to the interfacial damage (in the blue curve the degradation relation is not used). In other words, the active material particles become partly or fully (depending on the extent of the damage) isolated from the solid electrolyte. This reduction of the surface available for reaction, affects the charge transfer at the interface, the surface concentration increases faster and voltage drops quicker, therefore the capacity obtained becomes smaller.

In order to investigate the effect of C-rate on the damage evolution, the previous study is done using 2C and also 5C. The results are presented in Fig. 10. As shown in Fig. 10, at higher C-rates the cell potential drops faster and the delivered capacity is smaller, this happens even without the damage effect, which is mainly due to the quicker increase in the active material surface concentration (due to the bigger current), while the overall active material in the bulk is not lithiated yet. C-rate also affects the damage evolution. At higher C-rates damage starts earlier and evolves faster as well, since at higher C-rates the active material concentration increases faster, meaning the active material deforms quicker and therefore the mismatch and delamination at the interface starts earlier and evolve faster.

Finally the cell performance and the damage evolution for cells with different fracture energies (C-rate of 1) are plotted in Fig. 11. Here five values for the interface fracture energy are selected, namely $G_c \in \{13.92, 9, 5.97, 5, 4.21\}$ J/m^2. Three of these fracture energies $13.92, 5.97, 4.21$ J/m^2 are also the ones used for training the neural network and the other two are chosen arbitrarily from the range of the training data.

Fig. 11 shows that with smaller fracture energies (brittle interface), the damage starts earlier and grows faster and also has a final larger value in comparison to the cells with higher interface fracture energy (tough interface). This has to do with the fact that at the microscale for the interfaces with a smaller fracture energy, brittle interface, the damage evolution starts at smaller gaps at the interface in comparison to a tougher interface. Therefore, the capacity delivered by a cell with brittle interface is degraded more significantly in comparison to the capacity of a cell with a tough interface. The results suggest that the data-driven multiscale framework is capable of simulating the cell performance and damage evolution at different C-rates and even for fracture energies, with which it has not been trained. Furthermore the results suggest that influencing the interface fracture energy has a considerable effect on the interface delamination and the consequent contact loss and capacity fade in solid-state batteries.

Although the chemo-mechanical case was not simulated using the FE^2 method (due to very high computational costs), it is expected that the data-driven method is much more computationally efficient than the concurrent multiscale method. A comparison of the computation cost for the benchmark test is mentioned at the end of Section 3.1. The reason for the better computation performance is that in the FE^2 method for each integration point a finite element problem with thousands of degrees of freedom for the microscale is solved, while in our data-driven method only the neural network is called at each integration point.

4. Conclusions and future work

In this work, a data-driven multiscale framework is introduced to simulate the solid-state Li battery cell performance. The galvanostatic discharge process of the Li battery is modeled in two scales. At the macroscale, the mass balance for the lithium ion inside the electrolyte and the charge balance for both the electrolyte and the cathode active material are considered. This is done by implementing Nernst–Planck and Poisson equations. The balance of mass for the Li inside the cathode active material and its mechanical deformation are modeled at the microscale, where a chemo-mechanical coupled model is considered and the delamination at the interface of the active material and the solid electrolyte is modeled via the introduced cohesive zone model.
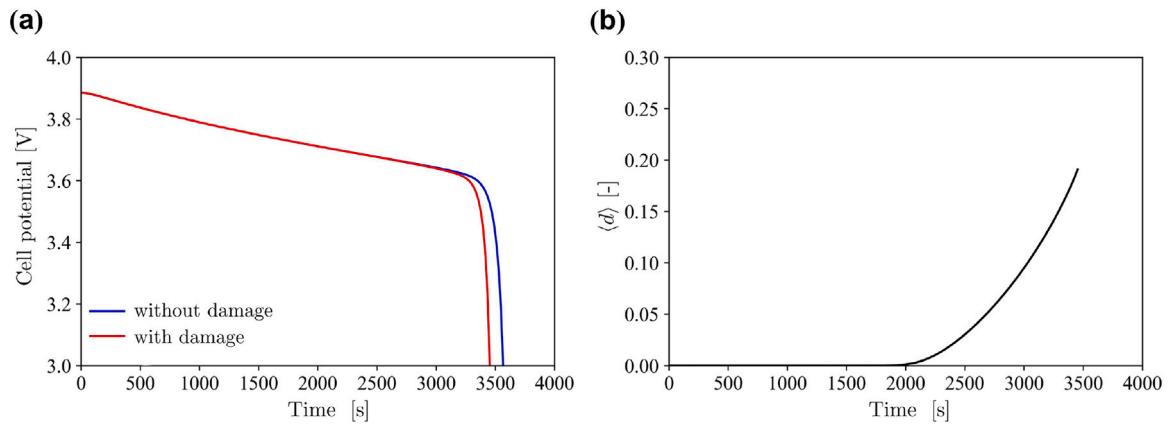
(a)

(b)

Fig. 9. Cell performance with and without the effect of damage and the damage evolution for a cell with $G_c = 5.97$ J/m^2.
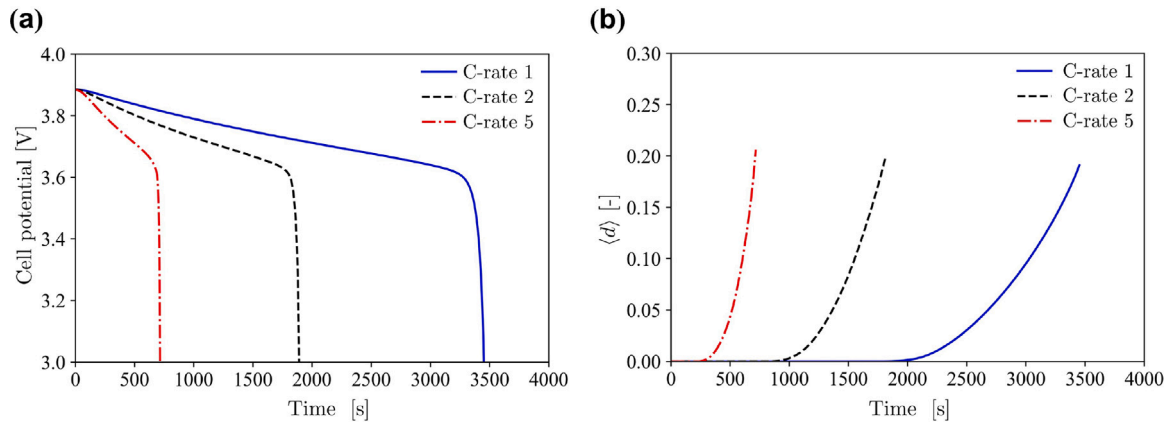
(a)

(b)

Fig. 10. Effect of C-rate on damage evolution.
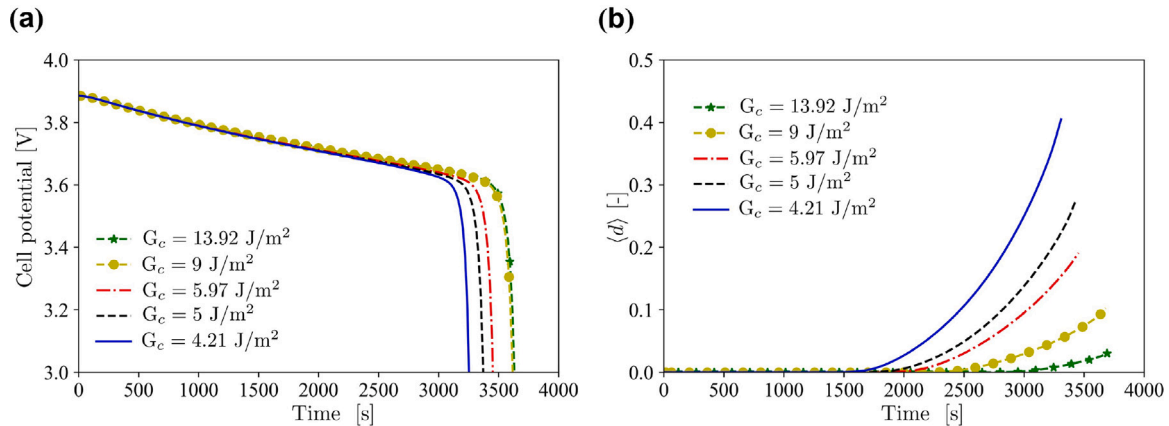
(a)

(b)

Fig. 11. Effect of fracture energy on cell performance and damage evolution.

Thanks to the multiscale approach, it is possible to simulate the cell performance in a multiphysics environment and consider the effect of deformation and interface damage on the cell performance. It is assumed that the interface damage reduces the active interfacial area between the electrolyte and the cathode active material. The sequential data-driven multiscale framework, introduced in this work, is benchmarked against the conventional concurrent method for a mechanically uncoupled example. Results show a good agreement between the two methods. However, the data-driven method has significantly higher efficiency and lower computation cost which is an advantage of this method. Using the data-driven method, one only needs to do microscale simulations individually once and then train an ML model based on that, which can be used in a macroscale cell model, and only cell simulations are now needed to get the cell performance under various conditions (based on the training data). Moreover, in this work, the data-driven approach is further developed to capture the interface delamination during the discharge process for cells with different fracture energies at the microscale. The surrogate model is capable of predicting the damage evolution even for unseen values of fracture energy. Through this approach, it is also possible to simulate the cell performance and the damage evolution under various conditions and C-rates. The results suggest that by discharging at higher C-rates the

interface delamination starts earlier and evolves quicker, which means the contact loss (between the active material and solid-electrolyte) occurs faster. Moreover, the fracture energy of the active material/ solid-electrolyte interface has a considerable effect on the interface delamination and contact loss and therefore the cell performance. The more brittle the interface is, the faster the damage evolves. This can be considered in material choice and design in aiming to produce cells with a longer lifetime and a robust contact between the active material and the solid-electrolyte.

For future work, one can suggest to investigate other machine learning approaches to develop a surrogate model for the sequential multiscale framework, such as Recurrent Neural Network, to account for the history effects. Moreover, one may integrate the governing equations (e.g. diffusion law) as an additional constraint to the network to make the predictions even more consistent with the underlying physics of the problem [56,64]. It is also of great interest to extend the surrogate model and consider more microscale material and geometrical properties in the development of the surrogate model so that more physical details are considered for the multiscale approach.

CRediT authorship contribution statement

Armin Asheri: Conceptualization, Methodology, Software, Writing – review & editing. **Mozhdeh Fathidoost:** Software, Writing – review & editing. **Vedran Glavas:** Supervision, Writing – review & editing. **Shahed Rezaei:** Conceptualization, Methodology, Supervision, Writing – review & editing. **Bai-Xiang Xu:** Methodology, Supervision, Writing – review & editing.

Declaration of competing interest

The authors declare that they have no known competing financial interests or personal relationships that could have appeared to influence the work reported in this paper.

Data availability

Data and related code are availabe at:

ML data and code (Original data) (GitHub).

Disclaimer

The results, opinions and conclusions expressed in this publication are not necessarily those of Volkswagen Aktiengesellschaft.

References

[1] F. Zhang, et al., A review of mechanics-related material damages in all-solid-state batteries: Mechanisms, performance impacts and mitigation strategies, Nano Energy 70 (2020) 104545.

[2] J. Ma, B. Chen, L. Wang, G. Cui, Progress and prospect on failure mechanisms of solid-state lithium batteries, J. Power Sources 392 (2018) 94–115.

[3] D. Andre, et al., Future generations of cathode materials: An automotive industry perspective, J. Mater. Chem. A 3 (13) (2015) 6709–6732.

[4] R. Koerver, et al., Capacity fade in solid-state batteries: Interphase formation and chemomechanical processes in nickel-rich layered oxide cathodes and lithium thiophosphate solid electrolytes, Chem. Mater. 29 (13) (2017) 5574–5582.

[5] P. Wang, et al., Electro–chemo–mechanical issues at the interfaces in solid-state lithium metal batteries, Adv. Funct. Mater. 29 (27) (2019) 1900950.

[6] R. Xu, et al., Heterogeneous damage in Li-ion batteries: Experimental analysis and theoretical modeling, J. Mech. Phys. Solids 129 (2019) 160–183.

[7] H.-H. Ryu, K.-J. Park, C.S. Yoon, Y.-K. Sun, Capacity fading of Ni-rich Li[Ni x Co y Mn 1–x–y]o2 (0.6 ≤ x ≤ 0.95) cathodes for high-energy-density lithium-ion batteries: Bulk or surface degradation? Chem. Mater. 30 (3) (2018) 1155–1163.

[8] H. Liu, et al., Intergranular cracking as a major cause of long-term capacity fading of layered cathodes, Nano Lett. 17 (6) (2017) 3452–3457.

[9] G. Sun, et al., On the fragmentation of active material secondary particles in lithium ion battery cathodes induced by charge cycling, Extreme Mech. Lett. 9 (2016) 449–458.

[10] H. Kim, M.G. Kim, H.Y. Jeong, H. Nam, J. Cho, A new coating method for alleviating surface degradation of LiNi0.6Co0.2Mn0.2O2 cathode material: Nanoscale surface treatment of primary particles, Nano Lett. 15 (3) (2015) 2111–2119.

[11] S. Rezaei, A. Asheri, B.-X. Xu, A consistent framework for chemo-mechanical cohesive fracture and its application in solid-state batteries, J. Mech. Phys. Solids 157 (2021) 104612.

[12] D. Bistri, A. Afshar, C.V. Di Leo, Modeling the chemo-mechanical behavior of all-solid-state batteries: A review, Meccanica 56 (2021) 1523–1554.

[13] Y. Luo, et al., Effect of crystallite geometries on electrochemical performance of porous intercalation electrodes by multiscale operando investigation, Nature Mater. (2022).

[14] S. Rezaei, A. Harandi, T. Brepols, S. Reese, An anisotropic cohesive fracture model: Advantages and limitations of length-scale insensitive phase-field damage models, Eng. Fract. Mech. 261 (2022) 108177.

[15] Y. Zhang, C. Zhao, Z. Guo, Simulation of crack behavior of secondary particles in Li-ion battery electrodes during lithiation/de-lithiation cycles, Int. J. Mech. Sci. 155 (2019) 178–186.

[16] G. Bucci, T. Swamy, Y.-M. Chiang, W.C. Carter, Modeling of internal mechanical failure of all-solid-state batteries during electrochemical cycling, and implications for battery design, J. Mater. Chem. A 5 (36) (2017) 19422–19430.

[17] R. Xu, K. Zhao, Corrosive fracture of electrodes in Li-ion batteries, J. Mech. Phys. Solids 121 (2018) 258–280.

[18] A. Singh, S. Pal, Coupled chemo-mechanical modeling of fracture in polycrystalline cathode for lithium-ion battery, Int. J. Plast. 127 (2020).

[19] L. Sultanova, Ł. Figiel, Microscale diffusion-mechanics model for a polymer-based solid-state battery cathode, Comput. Mater. Sci. 186 (2021) 109947.

[20] N. Iqbal, Y. Ali, I.U. Haq, S. Lee, Progressive interface debonding in composite electrodes of Li-ion batteries via mixed-mode cohesive zone model: Effects of binder characteristics, Compos. Struct. 259 (2021) 113173.

[21] Y. Bai, et al., A chemo-mechanical damage model at large deformation: Numerical and experimental studies on polycrystalline energy materials, Int. J. Solids Struct. (2021) 111099.

[22] M. Klinsmann, D. Rosato, M. Kamlah, R.M. McMeeking, Modeling crack growth during Li extraction and insertion within the second half cycle, J. Power Sources 331 (2016) 32–42.

[23] B.-X. Xu, Y. Zhao, P. Stein, Phase field modeling of electrochemically induced fracture in Li-ion battery with large deformation and phase segregation, GAMM-Mitt. 39 (1) (2016) 92–109.

[24] B. Liu, J. Xu, Cracks of silicon nanoparticles in anodes: Mechanics–electrochemical-coupled modeling framework based on the phase-field method, ACS Appl. Energy Mater. 3 (11) (2020) 10931–10939.

[25] A.M. Boyce, et al., Cracking predictions of lithium-ion battery electrodes by X-ray computed tomography and modelling, J. Power Sources 526 (2022) 231119.

[26] A. Mesgarnejad, A. Karma, Phase field modeling of chemomechanical fracture of intercalation electrodes: Role of charging rate and dimensionality, J. Mech. Phys. Solids 132 (2019) 103696.

[27] M. Doyle, T.F. Fuller, J. Newman, Modeling of galvanostatic charge and discharge of the lithium/polymer/insertion cell, J. Electrochem. Soc. 140 (6) (1993) 1526.

[28] J. Christensen, Modeling diffusion-induced stress in Li-ion cells with porous electrodes, J. Electrochem. Soc. 157 (3) (2010) A366.

[29] N. Wolff, F. Röder, U. Krewer, Model based assessment of performance of lithium-ion batteries using single ion conducting electrolytes, Electrochim. Acta 284 (2018) 639–646.

[30] S. Golmon, K. Maute, M.L. Dunn, Numerical modeling of electrochemical–mechanical interactions in lithium polymer batteries, Comput. Struct. 87 (23–24) (2009) 1567–1579.

[31] Y. Bai, Y. Zhao, W. Liu, B.-X. Xu, Two-level modeling of lithium-ion batteries, J. Power Sources 422 (2019) 92–103.

[32] P. Kumbhar, N. Swaminathan, R.K. Annabattula, Mesoscale analysis of Li-ion battery microstructure using sequential coupling of discrete element and finite element method, Int. J. Energy Res. 46 (9) (2022) 12003–12025.

[33] H. Fathiannasab, A.G. Kashkooli, T. Li, L. Zhu, Z. Chen, Three-dimensional modeling of all-solid-state lithium-ion batteries using synchrotron transmission X-ray microscopy tomography, J. Electrochem. Soc. 167 (10) (2020) 100558.

[34] J. Wegener, et al., Direct measurement of gaussian distributed radial crystallographic orientations of polycrystalline, layered-oxide secondary particles and their impact on materials utilization in battery cathodes, Energy Storage Mater. 45 (2022) 399–411.

[35] F. Fritzen, M. Hodapp, The finite element square reduced (FE2r) method with GPU acceleration: Towards three-dimensional two-scale simulations, Internat. J. Numer. Methods Engrg. 107 (10) (2016) 853–881.

[36] F. Feyel, Multiscale FE2 elastoviscoplastic analysis of composite structures, Comput. Mater. Sci. 16 (1–4) (1999) 344–354.

[37] F. Feyel, J.-L. Chaboche, FE2 multiscale approach for modelling the elastoviscoplastic behaviour of long fibre SiC/Ti composite materials, Comput. Methods Appl. Mech. Engrg. 183 (3–4) (2000) 309–330.

[38] R. Haj-Ali, D.A. Pecknold, J. Ghaboussi, G.Z. Voyiadjis, Simulated micromechanical models using artificial neural networks, J. Eng. Mech. 127 (7) (2001) 730–738.

[39] M.K. Mudunuru, et al., Surrogate models for estimating failure in brittle and quasi-brittle materials, Appl. Sci. 9 (13) (2019) 2706.

[40] D. Reimann, et al., Modeling macroscopic material behavior with machine learning algorithms trained by micromechanical simulations, Front. Mater. 6 (2019) 181.

[41] M. Fernández, S. Rezaei, J.R. Mianroodi, F. Fritzen, S. Reese, Application of artificial neural networks for the prediction of interface mechanics: A study on grain boundary constitutive behavior, Adv. Model. Simul. Eng. Sci. 7 (1) (2020) 1–27.

[42] J.R. Mianroodi, S. Rezaei, N.H. Siboni, B.-X. Xu, D. Raabe, Lossless multi-scale constitutive elastic relations with artificial intelligence, Npj Comput. Mater. 8 (1) (2022) 1–12.

[43] G.C. Peng, et al., Multiscale modeling meets machine learning: What can we learn? Arch. Comput. Methods Eng. 28 (2021) 1017–1037.

[44] J.S. Huang, J.X. Liew, A.S. Ademiloye, K.M. Liew, Artificial intelligence in materials modeling and design, Arch. Comput. Methods Eng. (2020).

[45] H. Salehi, R. Burgueño, Emerging artificial intelligence methods in structural engineering, Eng. Struct. 171 (2018) 170–189.

[46] M.-F. Ng, J. Zhao, G. Conduit, Z. Seh, Predicting the state of charge and health of batteries using data-driven machine learning, Nat. Mach. Intell. 2 (2020).

[47] L. Petrich, et al., Crack detection in lithium-ion cells using machine learning, Comput. Mater. Sci. 136 (2017) 297–305.

[48] Z. Jiang, et al., Machine-learning-revealed statistics of the particle-carbon/binder detachment in lithium-ion battery cathodes, Nature Commun. 11 (2020) 2310.

[49] Y.-C. Hsu, C.-H. Yu, M.J. Buehler, Using deep learning to predict fracture patterns in crystalline solids, Matter 3 (1) (2020) 197–211.

[50] J. Scharf, et al., Bridging nano-and microscale X-ray tomography for battery research by leveraging artificial intelligence, Nature Nanotechnol. (2022) 1–14.

[51] C. Bian, S. Yang, J. Liu, E. Zio, Robust state-of-charge estimation of Li-ion batteries based on multichannel convolutional and bidirectional recurrent neural networks, Appl. Soft Comput. (2022) 108401.

[52] J. Bao, et al., Machine learning coupled multi-scale modeling for redox flow batteries, Adv. Theory Simul. 3 (2) (2020) 1900167.

[53] G.H. Teichert, et al., Li_xCoO_2 phase stability studied by machine learning-enabled scale bridging between electronic structure, statistical mechanics and phase field theories, 2021.

[54] J. Wen, Q. Zou, Y. Wei, Physics-driven machine learning model on temperature and time-dependent deformation in lithium metal and its finite element implementation, J. Mech. Phys. Solids 153 (2021) 104481.

[55] S. Kohtz, Y. Xu, Z. Zheng, P. Wang, Physics-informed machine learning model for battery state of health prognostics using partial charging segments, Mech. Syst. Signal Process. 172 (2022) 109002.

[56] H.D. Deng, et al., Correlative image learning of chemo-mechanics in phase-transforming solids, Nature Mater. 21 (5) (2022) 547–554.

[57] A. Bhowmik, et al., A perspective on inverse design of battery interphases using multi-scale modelling, experiments and generative deep learning, Energy Storage Mater. 21 (2019) 446–456.

[58] R.G. Nascimento, M. Corbetta, C.S. Kulkarni, F.A. Viana, Hybrid physics-informed neural networks for lithium-ion battery modeling and prognosis, J. Power Sources 513 (2021) 230526.

[59] Y. Zhao, et al., Machine learning assisted design of experiments for solid state electrolyte lithium aluminum titanium phosphate, Front. Mater. 9 (2022) Art.–Nr.: 821817.

[60] H.S. Stein, et al., From materials discovery to system optimization by integrating combinatorial electrochemistry and data science, Curr. Opin. Electrochem. (2022) 101053.

[61] J. Newman, K.E. Thomas-Alyea, Electrochemical Systems, John Wiley & Sons, 2012.

[62] C. Cao, Z.-B. Li, X.-L. Wang, X.-B. Zhao, W.-Q. Han, Recent advances in inorganic solid electrolytes for lithium batteries, Front. Energy Res. 2 (2014) 25.

[63] T. Danner, et al., Thick electrodes for Li-ion batteries: A model based analysis, J. Power Sources 334 (2016) 191–201.

[64] S. Rezaei, A. Harandi, A. Moeineddin, B.-X. Xu, S. Reese, A mixed formulation for physics-informed neural networks as a potential solver for engineering problems in heterogeneous domains: Comparison with finite element method, 2022.

[65] D. Gaston, C. Newman, G. Hansen, D. Lebrun-Grandie, MOOSE: A parallel computational framework for coupled systems of nonlinear equations, Nucl. Eng. Des. 239 (10) (2009) 1768–1778.

[66] F. Chollet, et al., Keras, 2015, URL https://github.com/fchollet/keras.

[67] L. Buitinck, et al., API design for machine learning software: Experiences from the scikit-learn project, 2013, arXiv preprint arXiv:1309.0238.

[68] R. Xu, H. Sun, L.S. de Vasconcelos, K. Zhao, Mechanical and structural degradation of LiNixMnyCozO2 cathode in Li-ion batteries: An experimental study, J. Electrochem. Soc. 164 (13) (2017) A3333.

[69] R. Xu, H. Sun, L.S. de Vasconcelos, K. Zhao, Mechanical and structural degradation of LiNixMnyCozO2cathode in Li-ion batteries: An experimental study, J. Electrochem. Soc. 164 (13) (2017) A3333–A3341.

[70] R. Xu, L.S. de Vasconcelos, J. Shi, J. Li, K. Zhao, Disintegration of meatball electrodes for LiNixMnyCozO2 cathode materials, Exp. Mech. 58 (2018) 549–559.

[71] N. Legrand, et al., Including double-layer capacitance in lithium-ion battery mathematical models, J. Power Sources 251 (2014) 370–378.

[72] J.E. Ni, E.D. Case, J.S. Sakamoto, E. Rangasamy, J.B. Wolfenstine, Room temperature elastic moduli and Vickers hardness of hot-pressed LLZO cubic garnet, J. Mater. Sci. 47 (23) (2012) 7978–7985.

[73] R. Murugan, V. Thangadurai, W. Weppner, Fast lithium ion conduction in Garnet-type Li7La3Zr2O12, Angew. Chem. Int. Ed.s 46 (41) (2007) 7778–7781.